Materials Today Energy 12 (2019) 179–185

Contents lists available at ScienceDirect

Materials Today Energy

journal homepage: www.journals.elsevier.com/materials-today-energy/

Amorphous nickel boride membrane coated PdCuCo dendrites as high-efficiency catalyst for oxygen reduction and methanol oxidation reaction

Tingting Li [b, 1], Shuo Li [a, 1], Yunpeng Zuo [a], Guilin Zhu [a], Heyou Han [a, *]

[a] State Key Laboratory of Agricultural Microbiology, College of Science, Huazhong Agricultural University, Wuhan 430070, PR China
[b] Key Laboratory of Micro-Nano Materials for Energy Storage and Conversion of Henan Province, College of Advanced Materials and Energy, Institute of Surface Micro and Nano Materials, Xuchang University, Henan 461000, PR China

ARTICLE INFO

Article history:
Received 13 November 2018
Received in revised form
15 January 2019
Accepted 16 January 2019

Keywords:
Branched PdCuCo
Nickel boride membrane
Catalytic activity
Oxygen reduction reaction
Methanol oxidation reaction

ABSTRACT

Extensive efforts have been devoted to improve electrocatalytic activity of the catalysts in the fuel cells, however, it's still a big challenge to obtain the catalysts with low-cost and high-efficiency. Here we report the branched PdCuCo catalyst coated by amorphous nickel boride membrane displays an effective activity toward oxygen reduction reaction (ORR) and methanol oxidation reaction (MOR). The coating membrane serves as an electron acceptor to tune the surface electronic structure of the catalyst. And the interactional effect of the composite catalysts exhibit a normal distribution trend of mass activity (MA) and specific activity (SA) for the ORR and MOR. The SA of the composite catalysts effectively improves 3.3 times for ORR and 4.1 times for MOR than PdCuCo. Moreover, the proposed cost-effective catalyst can inspire novel design perspective about the focus attention of catalytic activity.

1. Introduction

As the most used catalysts in direct methanol fuel cell (DMFC), Pt-based nanocrystals are scarcity and highly cost [1–4]. Pd metal is considered a potential catalyst to replace Pt with the attractive performance for methanol oxidation reaction (MOR) and oxygen reduction reaction (ORR) [5,6]. However, there are also some challenges for monometallic Pd to use in DMFC compared with Pt, owing to its less electron transfer ability and inferior stability during catalytic process [7,8]. Extensive efforts have been devoted to modulate the electronic structure of Pd by alloying Pd with other transition metals. For example, Zhao and co-workers synthesized PdNi nanoparticles which represented better performance for the ethanol oxidation reaction than Pd/C [9]. Huang group developed ordered PdCu-based nanoparticles for ORR and ethanol-oxidation. They found that the compressive strain caused by the smaller atomic of Cu, Co, Ni and the ligand effect on the Pd surface can effectively improve its catalytic activity [10]. Consequently, alloying other low-cost transition metals to generate Pd-based catalysts is an appealing strategy to obtain high-efficiency DMFC catalysts.

The reactivity of the electro-catalysts highly relates to their surface arrangement of atoms. However, the stability is still a big challenge for highly active structures. In order to optimizing the catalytic efficiency of Pd-based electrocatalysts, many efforts have been devoted to tune particle structure and surface chemistry by diverse methods. For instance, Wen et al. reported (Zr, Ce)O_2 solid solution supported Pd cluster composite catalyst showed significantly improved catalytic activity for direct alcohol fuel cells [11]. Konda et al. employed a photoassisted method to directly decompose Pd nanoparticles onto g-C_3N_4 as high-efficiency catalyst for ORR [8]. Xiao et al. reported the particle size and surface strain of Pd nanocatalyst can be effectively regulated by introducing Fe and Co into the Pd lattice, which exhibited excellent catalytic activity for ORR [12]. In addition to the above-mentioned approaches, surface compositional modulation has been proved great importance to boost catalytic activity [13]. Typically, core-shell $Pd_1Ru_1Ni_2$@Pt/C catalyst displayed enhanced ORR activity due to the strong electron interactions between the core and shell [14]. However, the above catalysts are either expensive or require harsh preparation techniques and conditions, which is quite limited in practical applications. Therefore, a electrocatalyst, which is cost-effective and easily

* Corresponding author.
E-mail address: hyhan@mail.hzau.edu.cn (H. Han).
[1] These authors contributed equally to this work.

https://doi.org/10.1016/j.mtener.2019.01.007
2468-6069/

available but still possesses excellent activity for certain catalytic processes, is urgently needed.

Recently, amorphous alloys, with the isotropic and homogeneous characters, can exhibit a uniform dispersion of active sites and high density of coordinatively unsaturated sites (CUSs), which is very attractive for the development of catalysts with exclusive activity [15–17]. Nonetheless, individualized amorphous alloy maybe limited directly as electrocatalyst due to the insufficient active sites and inconspicuous charge effect. Impressively, integrating metal crystal with amorphous alloy has a synergistic effect, which can manifest highly dispersed active surface and 'crystal-amorphous' interface electron interaction to enhance electrocatalytic activity [18,19].

Herein, we present an interactional effect between a crystalline surface of branched PdCuCo alloy and amorphous Ni-B membrane which displays highly efficient catalytic activity toward ORR and MOR. A series of PdCuCo/Ni-B were synthesized via simple chemical reduction with a gradient of $NaBH_4$ and $Ni(NO_3)_2$ solution to further investigate the dependence of intrinsic electrocatalytic activity on different thickness of Ni-B membrane. Furthermore, the close interaction and interfaces between branched PdCuCo alloy and amorphous Ni-B membrane play key role in modulating the catalytic activity for the ORR and MOR.

2. Experimental section

2.1. Materials

Hexadecyltrimethylammonium bromide (CTAB, Sigma-Aldrich, 99.0%), ascorbic acid (AA, Sinopharm, 99.7%), potassium bromide (KBr, Guangfubiaowu, 99.5%), sodium tetrachloropalladate (Na_2PdCl_4, Aladdin, 98.0%), sodium borohydride ($NaBH_4$, Sinopharm, 96.0%), copper(II) nitrate trihydrate ($Cu(NO_3)_2{\cdot}3H_2O$, Sinopharm, 99.0%), cobalt(II) nitrate hexahydrate ($Co(NO_3)_2{\cdot}6H_2O$, Sinopharm, 99.0%), nickel(II) nitrate hexahydrate ($Ni(NO_3)_2{\cdot}6H_2O$, Sinopharm, 98.0%). Ultrapure water (resistance = 18.2 MΩ/cm) was used in all experiments.

2.2. Synthesis of branched PdCuCo alloy

Firstly, 0.5 g of CTAB, 0.45 g of AA and 0.25 g of KBr were dissolved into 30 mL of water. The solution was stirred for 5 min before the addition of 3 mL of Na_2PdCl_4 (33.98 mM), 0.9 mL of $Cu(NO_3)_2$ (48 mM) and 0.2 mL of $Co(NO_3)_2$ (48 mM) at room temperature. Then, the mixture was continuously stirred for 60 min at 100 °C sand-bath condition. The black product was centrifuged at 10000 rpm for 10 min and was washed with water twice. At last, the as-synthesized branched PdCuCo alloy were dispersed into 10 mL of water for future investigation.

2.3. Synthesis of branched PdCuCo/Ni-B composite

1 mL of as-synthesized branched PdCuCo alloy aqueous solution and 10 mg/mL $Ni(NO_3)_2$ solution was first mixed and kept stirring for 5 min, followed by introducing a fresh 20 mg/mL $NaBH_4$ solution under ultrasonication. After stirring for another 15 min, the as-prepared products were collected after washing twice by water and centrifugation. To synthesize a series of PdCuCo/Ni-B with different thickness of Ni-B membrane, a gradient of $NaBH_4$ and $Ni(NO_3)_2$ solution were added into reaction systems (Table S1).

2.4. Materials characterizations

Size, morphology, element composition, and microstructure of samples were characterized by transmission electron microscope (TEM, JEM-2010FEF) and high-resolution transmission electron microscopy (HRTEM, FEI Talos F200C at 200 kV) equipped with a scanning transmission electron microscopy (STEM) detector and a selected-area electron diffraction (SAED) accessory. The crystal structure, surface chemical state, and electronic structure of samples were analyzed by X-ray diffraction (XRD, Bruker D8) and X-ray photoelectron spectroscopy (XPS, Thermo VG Multilab 2000 spectrometer with a monochromatic Al Kα radiation source) technique.

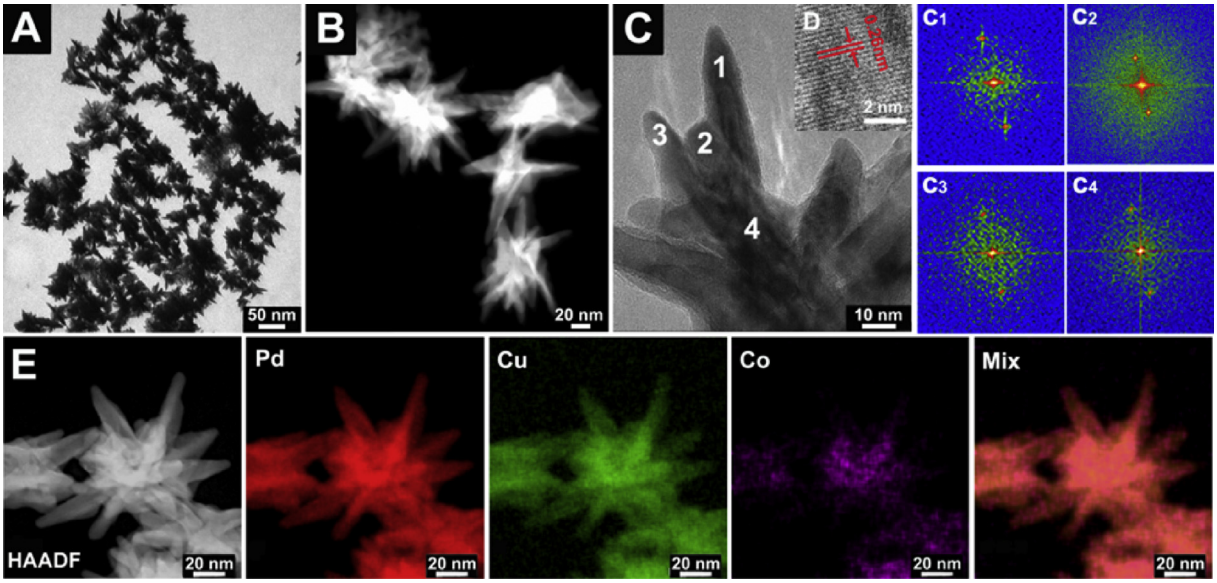

Fig. 1. (A) TEM and (B) High-angle annular dark-field scanning transmission electron microscope (HAADF-STEM) images of PdCuCo. (C) Corresponding HRTEM image and (D) lattice image. (C_1–C_4)–The different areas of fast Fourier-transformed (FFT) images corresponding to the digitally labeled in (C). (E) The typical HAADF-STEM image and the corresponding STEM-EDS elemental mapping of branched PdCuCo alloy.

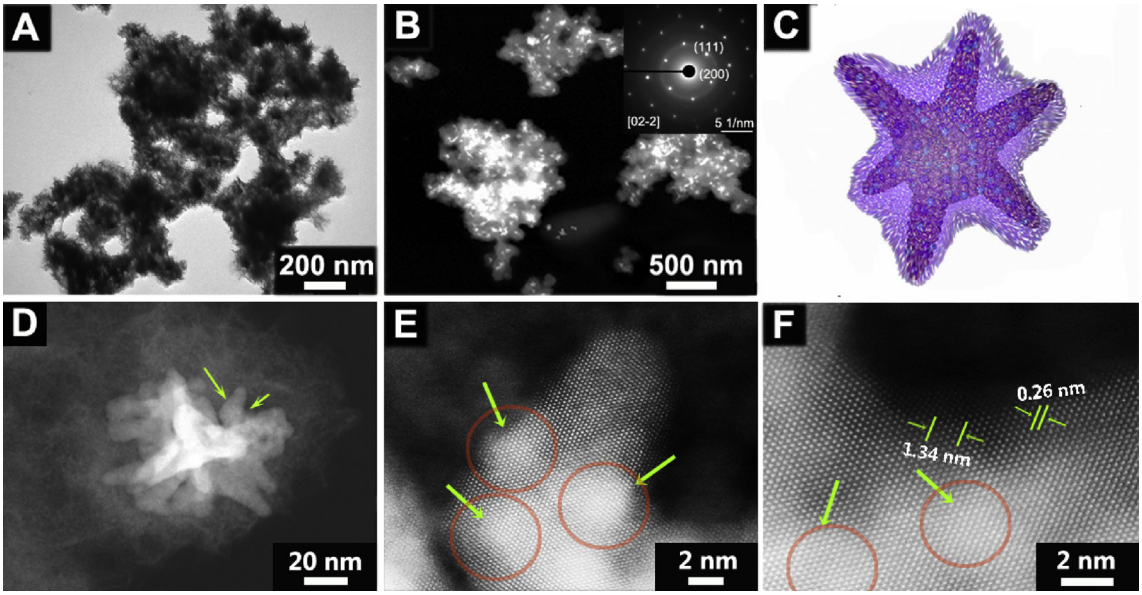

Fig. 2. (A) TEM image of PdCuCo/Ni-B-3. (B, D) HAADF-STEM images of PdCuCo/Ni-B-3. The inset in Fig. 2B shows the SAED pattern. (C) The simulative structure of PdCuCo/Ni-B-3 composite. (E, F) Atomic-resolution HAADF-STEM images of PdCuCo/Ni-B-3 composite.

2.5. Electrochemical measurements

Cyclic voltammetry (CV) and ORR polarization measurements were carried out on the CHI 660B electrochemical workstation (CH Instruments, Chenhua Co., Shanghai, China) with the Pine AFMSRCE rotating disk electrode at 25 ± 1 °C. For all electrochemical experiments, a single-compartment three electrode electrochemical cell was used, which included a saturated calomel reference electrode, a Pt wire auxiliary electrode, and a catalyst-modified working electrode. All potentials in this work were referred to the reversible hydrogen electrode (RHE). CV tests were performed at room temperature in N_2-purged 0.1 M $HClO_4$ solution with a sweep rate of 50 mV/s. The ORR activity was measured in the potential range of −0.2–0.95 (V vs. RHE) in O_2-saturated 0.1 M $HClO_4$ solution with a sweep rate of 10 mV/s and a rotation rate of 1600 rpm. The MOR activity was measured in the potential range of −0.7–0.3 (V vs. RHE) in 1.0 M KOH and 1.0 M CH_3OH solution with a sweep rate of 50 mV/s.

3. Results and discussion

The structure of PdCuCo alloy was first characterized shown in Fig. 1. TEM and HAADF-STEM images clearly revealed the branched morphology of PdCuCo with divergent thorn-like structures (Fig. 1A and B). The growth homogeneity along each branch can be reflected distinctly from their similar FFT images presented in Fig. 1C_1–C_4. In the HRTEM image of Fig. 1D, lattice distance of 0.26 nm is well consistent with the (100) plane of fcc PdCu [20,21]. The STEM image and corresponding elemental mapping shows homogeneous distribution of Pd and Cu elements in the whole branched structure with a small amount of Co (Fig. 1E). This observation is also consistent with ICP-MS results displayed in Table S2.

Fig. 2A shows the TEM images of PdCuCo/Ni-B-3 obtained by integrating the crystalline branched PdCuCo with amorphous Ni-B alloy. It was speculated that branched PdCuCo alloy would undergo a encapsulated process by an amorphous Ni-B membrane, which was induced by the Ni^{2+} and active $NaBH_4$. Fig. 2B and D are the

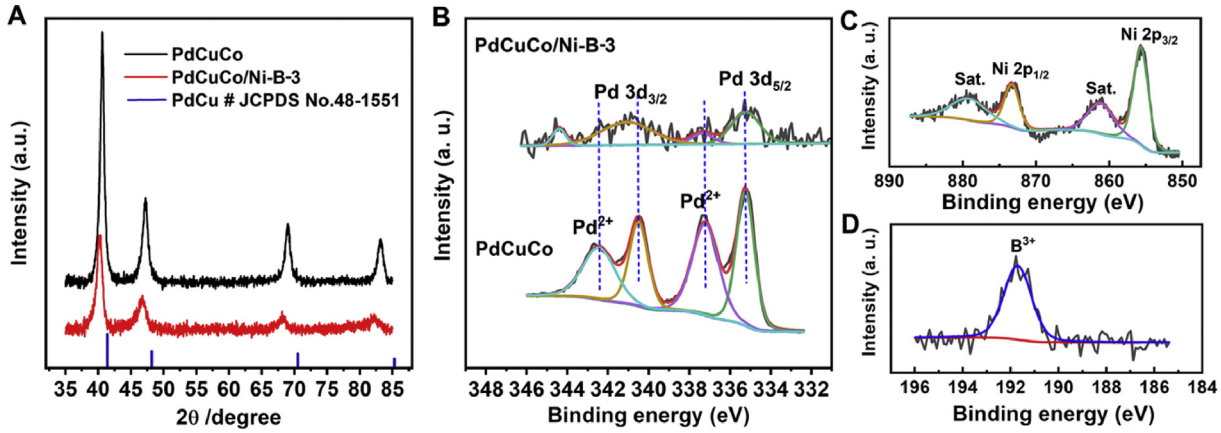

Fig. 3. (A) XRD patterns of PdCuCo, PdCuCo/Ni-B-3 and JCPDS data of PdCu for comparison. (B) Pd 3d XPS spectra of PdCuCo and PdCuCo/Ni-B-3. (C) Ni 2p and (D) B 1s XPS spectra of PdCuCo/Ni-B-3.

HAADF-STEM images of as-obtained hybrid PdCuCo/Ni-B-3 structures. As can be seen, the amorphous layer with disordered lattice successfully coated on PdCuCo alloy surface. Interestingly, benefiting from its isotropic structure feature, the formed Ni-B membrane can promote the efficient diffusion of ions during electrochemical reaction process while maintaining the structure stability [22]. Additionally, the crystalline branched PdCuCo alloy was also clearly observed from bright branched nanocrystal, which was surrounded by the gray amorphous Ni-B membrane. The visual structural models presented in Fig. 2C. SAED pattern (inset in Fig. 2B) shows the single crystalline nature of PdCuCo with [111] and [200] lattice planes of PdCu cubic phase. Moreover, The lattice spacing corresponding to PdCu alloy shown in Fig. 2F is 0.26 nm, closing to that of the (200) plane of PdCu alloy (0.265 nm). This confirmed the coated Ni-B membrane does not disrupt the crystalline structure of PdCuCo alloy. In addition, the bright spot areas appear in the atomic-resolution HAADF-STEM images (marked by the green arrows in Fig. 2D, E and F) may be due to the crystallization of Ni-B membrane caused by electron beam irradiation. A similar phenomenon is also found from the HRTEM image of PdCuCo/Ni-B-4 (Fig. S1), in which the crystal particles associated with Ni-B membrane pointed out by the green arrows were observed after undergoing prolonged electron beam irradiation.

XRD were performed to elucidate the crystalline structure and phase evolution induced by Ni-B membrane cladding (Fig. 3A). PdCuCo and PdCuCo/Ni-B-3 show four typical diffraction peaks assigned to (111), (200), (220) and (311) of PdCu fcc structure with slight low-angle shift compared with the Joint Committee on Powder Diffraction Standards (JCPDS) data (48-1551) [7]. The slight shift for former caused by the incorporation of Co atoms [23]. The further shift for latter implies the close interaction between branched PdCuCo alloy and amorphous Ni-B membrane. No

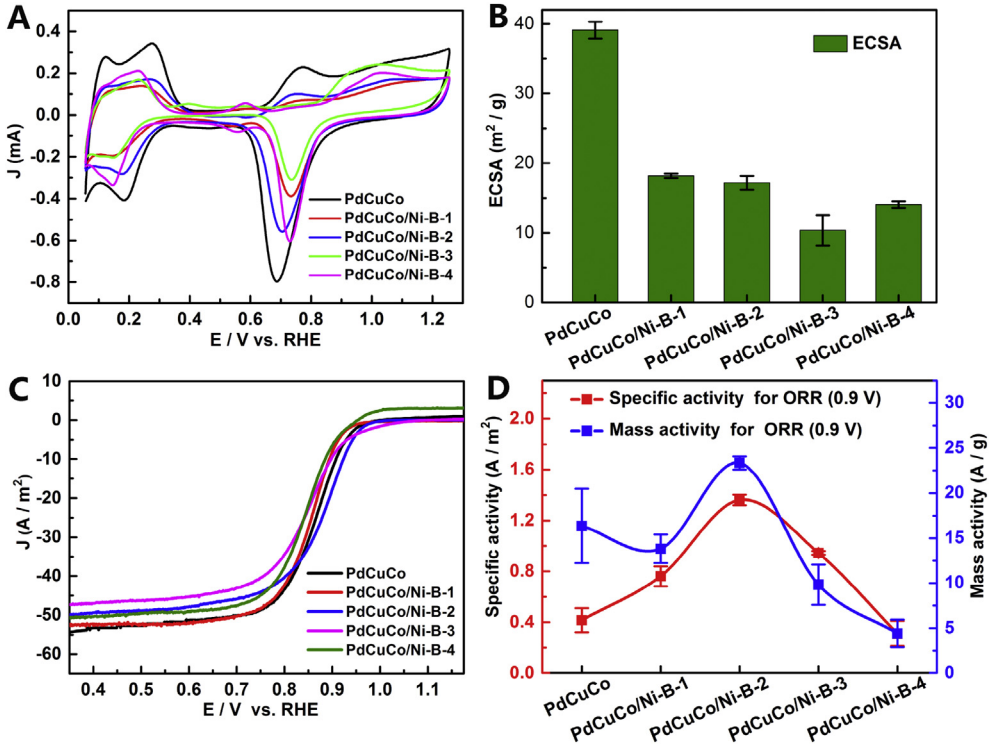

Fig. 4. Electrocatalytic performance of PdCuCo and PdCuCo/Ni-B. (A) CVs recorded at room temperature in a N_2-saturated 0.1 M $HClO_4$ solution at a sweep rate of 50 mV/s (B) ECSAs of PdCuCo and PdCuCo/Ni-B. (C) ORR polarization curves recorded at room temperature in an O_2-saturated 0.1 M $HClO_4$ aqueous solution at a sweep rate of 10 mV/s and a rotation rate of 1600 rpm. The currents were normalized to the geometric area of the rotating disk electrode (0.196 cm^2). (D) Mass activity (MA) and specific activity (SA) of PdCuCo and PdCuCo/Ni-B for ORR at 0.9 V_{RHE}. The error bars represent the standard deviations of three samples.

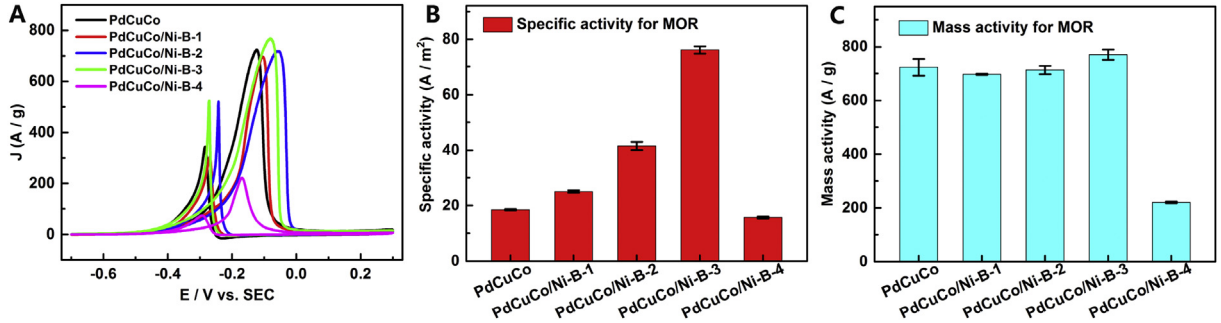

Fig. 5. Electrocatalytic performance of PdCuCo and PdCuCo/Ni-B for MOR. (A) Pd mass normalized CV curves of PdCuCo and PdCuCo/Ni-B in 1.0 M KOH electrolyte solutions containing 1.0 M methanol with sweep rate of 50 mV/s (B) SA (normalized against ECSA), and (C) MA (normalized against Pd mass) of PdCuCo and PdCuCo/Ni-B. The error bars represent the standard deviations of three samples.

diffraction peaks corresponding to Co species were detected due to the low content (Table S2). Besides, the diffraction peaks of PdCuCo exhibit stronger intensity over PdCuCo/Ni-B-3, indicating the insufficient expose of crystal plane after Ni-B membrane coating [24]. Naturally, no other peaks associated with Ni-B membrane was found for PdCuCo/Ni-B-3 due to the amorphous nature. However, their existence and composition can be intuitively confirmed from the TEM observation and XPS characterization. As shown in Fig. 3B, the Pd 3d XPS spectra were fitted by four core-level curves with more intensive peaks belong to metallic palladium for both PdCuCo and PdCuCo/Ni-B-3 [25,26]. Compared with PdCuCo, the binding energy of Pd 3d for PdCuCo/Ni-B-3 up-shifted, implicating the electron-donating properties of Pd. The Ni 2p XPS spectra of PdCuCo/Ni-B-3 shown in Fig. 3C reveal that the existent state are mainly in oxidation state rather than metal atoms, which can serve as electron receptor to modulates the catalytic activity of catalysts. As shown in Fig. 3D, the peak at 191.7 eV of B 1s spectra corresponds to the boron oxide. Notably, the electron-deficient property of boron derived from the oxidation with air exposure or partial electron transfer to the alloying Ni. Merely, the latter effect is not obvious because of the scant coordination number of Ni-B [27,28]. These findings together suggest the interactions with the electron transfer tendency from active catalyst to Ni-B membrane. The formation of boron oxide would play an important role in boosting the electrocatalytic activity [29]. Co XPS spectra of PdCuCo/Ni-B-3 was shown in Fig. S2.

We evaluated the catalytic activities of both of the PdCuCo and PdCuCo/Ni-B toward ORR. Fig. 4A shows cyclic voltammograms (CVs) of different types of catalysts at room temperature in N_2-saturated 0.1 M $HClO_4$ solutions at a sweeping rate of 50 mV/s in the potential range of 0.056–1.256 V versus reversible hydrogen electrode (RHE). As a result, the specific electrochemical active surface areas (ECSAs) derived from the charges responsible for the H_{upd} desorption between 0.056 and 0.456 V (versus RHE) and normalized to the Pd mass was shown in Fig. 4B. The corresponding values were listed in Table S3. Naturally, PdCuCo possessed higher specific ECSA (39.10 m^2/g) than that of other catalysts due to the original exposure of multi-branch morphology and low palladium content (Table S2). Fig. 4C shows the positive-going ORR polarization curves of PdCuCo and PdCuCo/Ni-B catalysts. PdCuCo/Ni-B-2 showed relatively better ORR performance, as reflected from its more positive half-wave ($E_{1/2}$) potentials (0.881 V vs. RHE). The mass and specific activities ($j_{k,mass}$ and $j_{k,specific}$) were calculated using the Koutecky-Levich equation and then normalized against the ECSA and Pd mass of the catalyst. Fig. 4D shows the SA and MA of PdCuCo and PdCuCo/Ni-B for ORR at 0.9 V vs. RHE. The definite values are also presented (Table S4). Obviously, the catalytic performance of PdCuCo/Ni-B-2 outperforms over other catalysts with a MA value of 23.3 A/g_{Pd} and SA value of 1.3612 A/m^2. Compared to commercial Pd/C (MA = 10.166 A/g_{Pd} and SA = 0.4446 A/m^2, Table S6), the catalytic performance of PdCuCo/Ni-B-2 also have a greatly improvement. The superior activity of PdCuCo/Ni-B-2 benefits from the close interaction of crystal PdCuCo and amorphous Ni-B membrane, as well as the synergistically modulated interface electronic structure. Moreover, the comparison also indicates that the coating thickness of Ni-B membrane greatly affects the catalytic performance. The catalytic durability of PdCuCo/Ni-B-2 was further evaluated by the amperometric measurement at 0.6 V (vs RHE) in the O_2-saturated 0.1 M $HClO_4$ aqueous solution at rotation rate of 1600 rpm (Fig. S4). It shows that PdCuCo/Ni-B-2 have better durability compared to PdCuCo and Pd/C catalyst.

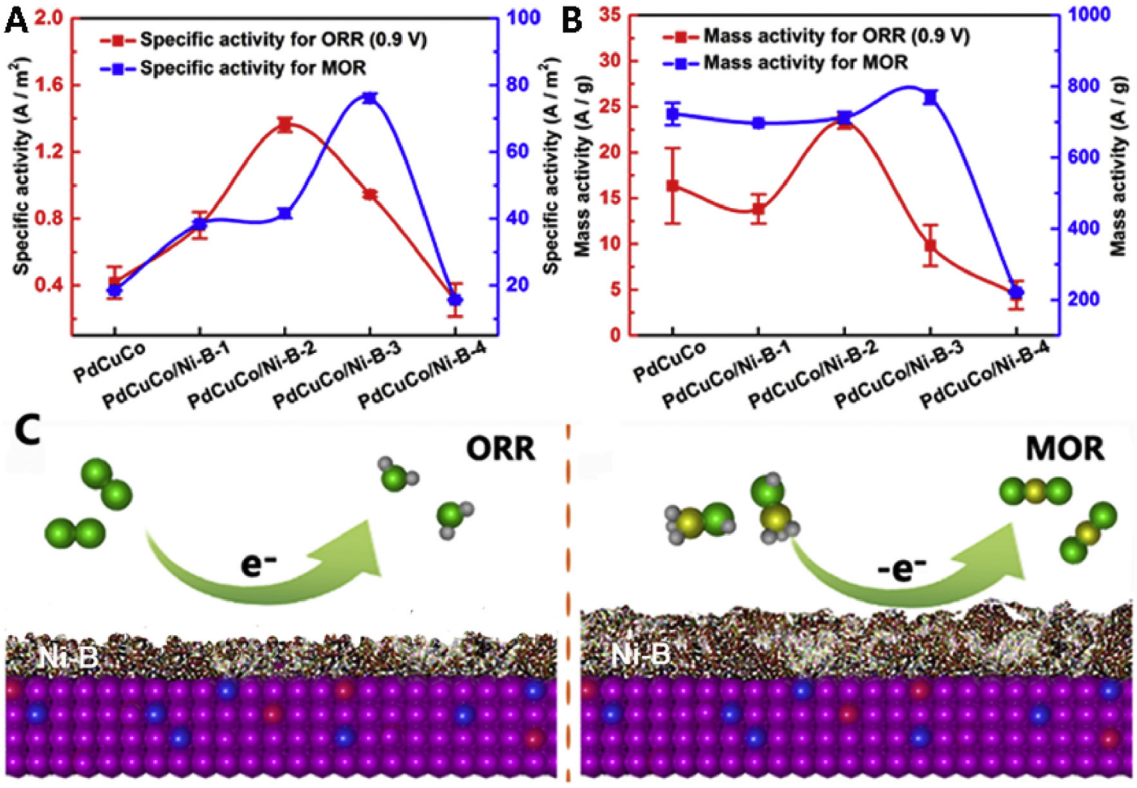

Fig. 6. MA and SA of PdCuCo and PdCuCo/Ni-B for ORR and MOR. (A) SA for ORR at 0.9 V_{RHE} and MOR. (B) MA for ORR at 0.9 V_{RHE} and MOR. The error bars represent the standard deviations of three samples. (C) Side views of the catalytic transformation of PdCuCo/Ni-B for ORR and MOR model surfaces (pink ball:Pd; red ball:Co; blue ball:Cu; green ball:O; gray ball:H; yellow ball:C).

The electrocatalytic activity of PdCuCo and PdCuCo/Ni-B were further evaluated for MOR. Fig. 5A shows the representative CVs normalized with the mass of Pd in the solution of 1.0 M KOH and 1.0 M CH_3OH at 50 mV/s. As observed, the peak current of PdCuCo/Ni-B-3 presented a highest value of 717.04 A/g_{Pd}, indicating effective enhancement in catalytic activity due to the coating of Ni-B membrane. Furthermore, PdCuCo/Ni-B-3 also displayed the highest specific and mass activity among all catalysts (Fig. 5B and C). Table S5 shows the calculated values of the activity for each catalyst. Compared to commercial Pd/C (MA = 408 A/g_{Pd} and SA = 14.8922 A/m^2, Table S6), the catalytic activity of PdCuCo/Ni-B-3 for MOR also show an effective enhancement. The aforementioned results not only clarify the coordinated effect between different composition and heterogenous interface, but also implies that the coating amount of Ni-B membrane is an important impact parameter for the catalytic activity. Based on previous analysis, the enhanced electrocatalytic activity can be attributed to the highly multi-branched structure with large active surface area and synergistic electronic interaction between the active surface and Ni-B membrane. Interestingly, the coating amount of Ni-B membrane is not the more the better according to the test results. It implies the significant dependence of electrocatalytic activity toward MOR on the Ni-B coating thickness.

To further explore the modulation mechanism and catalytic characteristics of the synthesized catalysts, the corresponding electrocatalytic activity for ORR and MOR are summarized together to intuitive comparison, as shown in Fig. 6A and B. PdCuCo/Ni-B-1 showed downgrade MA compared with PdCuCo as a result of reduced utilization ratio of palladium active sites after buried inside the Ni-B membrane. Besides, the small amount of incomplete or uneven coating leads to inconspicuous synergistic effect between the crystal PdCuCo and amorphous Ni-B membrane [30]. Further increased coating thickness can lead to more dense coating based on the macroscopic view, which is unfavorable for the moleculars or ions transfer. Consequently, the catalytic activity of PdCuCo/Ni-B for ORR and MOR shows a trend of increasing first and then weakening with the increase in the coating amount of Ni-B membrane. The theoretical calculation confirm the dominating effect of electron-deficient Ni-B membrane, which can modulate electron transfer of composite and electron structure of active Pd surface [29]. Additionally, moderate strength adsorption between catalysts and reactants or products endows high catalytic activity follow the volcano-shaped curve [31]. As shown in Fig. 6C, PdCuCo/Ni-B-2 exhibited much higher catalytic activity for ORR and PdCuCo/Ni-B-3 represent better performance for MOR.

4. Conclusion

In summary, Pd-based multi-branch crystal covered by novel amorphous membrane was successfully fabricated by simple wet-chemical technique. Due to the unique alloy synergies, open branched structure and positive crystalline-amorphous interface electron effect, the prepared PdCuCo/Ni-B exhibit highly efficient catalytic performance for ORR and MOR. Intriguingly, gaussian-like activity distribution curves were observed with different thickness of Ni-B membrane coating. Particularly, The SA of PdCuCo/Ni-B were 3.3 times and 4.1 times higher than that of PdCuCo for ORR and MOR, respectively. This study may inspire more rational design associated with amorphous hybrid nanomaterials for extensive application in the future.

Conflicts of interest

The authors declare no conflict of interest.

Acknowledgments

This work is supported by the National Natural Science Foundation of China (21778020), National Key R&D Program of China (2016YFD0500706), Science and Technology Major Project of Guangxi (Gui Ke AA18118027), Sci-tech Innovation Foundation of Huazhong Agriculture University (2662017PY042, 2662018PY024), Scientific and Technological Projects of Henan Province (182102210502), and Education Department of Henan Province (18A430003). Part of Microscopy studies were accomplished at the Analytical and Testing Center of Huazhong Agricultural University (HZAU) for field emission TEM testing. We thank Limin He and Jianbo Cao for their help on TEM work at HZAU.

Appendix A. Supplementary data

Supplementary data to this article can be found online at https://doi.org/10.1016/j.mtener.2019.01.007.

References

[1] M.E. Scofield, H. Liu, S.S. Wong, A concise guide to sustainable PEMFCs: recent advances in improving both oxygen reduction catalysts and proton exchange membranes, Chem. Soc. Rev. 44 (2015) 5836–5860.
[2] L. Zhang, X.-F. Zhang, X.-L. Chen, A.-J. Wanga, D.-M. Han, Z.-G. Wanga, J.-J. Feng, Facile solvothermal synthesis of Pt71Co29 lamellar nanoflowers as an efficient catalyst for oxygen reduction and methanol oxidation reactions, J. Colloid Interface Sci. 536 (2019) 556–562.
[3] Y.-C. Shi, L.-P. Mei, A.-J. Wang, T. Yuan, S.-S. Chen, J.-J. Feng, *L*-Glutamic acid assisted eco-friendly one-pot synthesis of sheet assembled platinum-palladium alloy networks for methanol oxidation and oxygen reduction reactions, J. Colloid Interface Sci. 504 (2017) 363–370.
[4] L.-Y. Jiang, X.-Y. Huang, A.-J. Wang, X.-S. Li, J. Yuan, J.-J. Feng, Facile solvothermal synthesis of $Pt_{76}Co_{24}$ nanomyriapods for efficient electrocatalysis, J. Mater. Chem. A 5 (2017) 10554–10560.
[5] M. Shao, Palladium-based electrocatalysts for hydrogen oxidation and oxygen reduction reactions, J. Power Sources 196 (2011) 2433–2444.
[6] S.K. Konda, M. Amiri, A. Chen, Photoassisted deposition of palladium nanoparticles on carbon nitride for efficient oxygen reduction, J. Phys. Chem. C 120 (2016) 14467–14473.
[7] Z. Chen, Y.-C. He, J.-H. Chen, X.-Z. Fu, R. Sun, Y.-X. Chen, C.-P. Wong, PdCu alloy flower-like nanocages with high electrocatalytic performance for methanol oxidation, J. Phys. Chem. C 122 (2018) 8976–8983.
[8] C. Alegre, A. Stassi, E. Modica, C.L. Vecchio, A.S. Aricò, V. Baglio, Investigation of the activity and stability of Pd-based catalysts towards the oxygen reduction (ORR) and evolution reactions (OER) in iron-air batteries, RSC Adv. 5 (2015) 25424–25427.
[9] S.Y. Shen, T.S. Zhao, J.B. Xu, Y.S. Li, Synthesis of PdNi catalysts for the oxidation of ethanol in alkaline direct ethanol fuel cells, J. Power Sources 195 (2010) 1001–1006.
[10] K. Jiang, P. Wang, S. Guo, X. Zhang, X. Shen, G. Lu, D. Su, X. Huang, Ordered PdCu-based nanoparticles as bifunctional oxygen-reduction and ethanol-oxidation electrocatalysts, Angew. Chem. Int. Ed. 128 (2016) 1–7.
[11] C. Wen, Y. Wei, D. Tang, B. Sa, T. Zhang, C. Chen, Improving the electrocatalytic properties of Pd-based catalyst for direct alcohol fuel cells: effect of solid solution, Sci. Rep. 7 (2017) 1–11.
[12] W. Xiao, M.A.L. Cordeiro, M. Gong, L. Han, J. Wang, C. Bian, J. Zhu, H. Xin, D. Wang, Optimizing the oxygen reduction reaction activity of Pd based nanocatalyst by tuning strain and particle size, J. Mater. Chem. A 5 (2017) 9867–9872.
[13] M. Wang, Z. Ma, R. Li, B. Tang, X.-Q. Bao, Z. Zhang, X. Wang, Novel flower-like PdAu(Cu) anchoring on a 3D rGO-CNT sandwich-stacked framework for highly efficient methanol and ethanol electro-oxidation, Electrochim. Acta 227 (2017) 330–344.
[14] H. Nan, X. Tian, J. Luo, D. Dang, R. Chen, L. Liu, X. Li, J. Zeng, S. Liao, A core-shell $Pd_1Ru_1Ni_2$@Pt/C catalyst with a ternary alloy core and Pt monolayer: enhanced activity and stability towards the oxygen reduction reaction by the addition of Ni, J. Mater. Chem. A 4 (2016) 847–855.
[15] Á. Molnár, G.V. Smith, M. Bartók, New catalytic materials from amorphous metal alloys, Adv. Catal. 36 (1989) 329–383.
[16] A. Baiker, Metallic glasses in heterogeneous catalysis, Chem. Soc. 87 (1989) 239–251.
[17] Y. Pei, G. Zhou, N. Luan, B. Zong, M. Qiao, F.F. Tao, Synthesis and catalysis of chemically reduced metal-metalloid amorphous alloys, Chem. Soc. Rev. 41 (2012) 8140–8162.
[18] S.-J. Zhang, Y.-X. Zheng, L.-S. Yuan, L.-H. Zhao, Ni-B amorphous alloy nanoparticles modified nanoporous Cu toward ethanol oxidation in alkaline medium, J. Power Sources 247 (2014) 428–436.

[19] N. Xu, G. Cao, Z. Chen, Q. Kang, H. Dai, P. Wang, Cobalt nickel boride as an active electrocatalyst for water splitting, J. Mater. Chem. A 5 (2017) 12379–12384.
[20] Y. Zuo, D. Rao, S. Li, T. Li, G. Zhu, S. Chen, L. Song, Y. Chai, H. Han, Atomic vacancies control of Pd-based catalysts for enhanced electrochemical performance, Adv. Mater. 30 (2018) 1704171.
[21] K.A. Goulas, S. Sreekumar, Y. Song, P. Kharidehal, G. Gunbas, P.J. Dietrich, G.R. Johnson, Y.C. Wang, A.M. Grippo, L.C. Grabow, A.A. Gokhale, F.D. Toste, Synergistic effects in bimetallic palladium-copper catalysts improve selectivity in oxygenate coupling reactions, J. Am. Chem. Soc. 138 (2016) 6805–6812.
[22] S. Sun, T. Zhai, C. Liang, S.V. Savilov, H. Xia, Boosted crystalline/amorphous $Fe_2O_{3-\delta}$ core/shell heterostructure for flexible solid-state pseudocapacitors in large scale, Nano Energy 45 (2018) 390–397.
[23] C. Xu, Y. Liu, J. Wang, H. Geng, H. Qiu, Nanoporous PdCu alloy for formic acid electro-oxidation, J. Power Sources 199 (2012) 124–131.
[24] Q. Hua, D. Shang, W. Zhang, K. Chen, S. Chang, Y. Ma, Z. Jiang, J. Yang, W. Huang, Morphological evolution of Cu_2O nanocrystals in an acid Solution: stability of different crystal planes, Langmuir 27 (2011) 665–671.
[25] N. Yang, Z. Zhang, B. Chen, Y. Huang, J. Chen, Z. Lai, Y. Chen, M. Sindoro, A.-L. Wang, H. Cheng, Z. Fan, X. Liu, B. Li, Y. Zong, L. Gu, H. Zhang, Synthesis of ultrathin PdCu alloy nanosheets used as a highly efficient electrocatalyst for formic acid oxidation, Adv. Mater. 29 (2017) 1700769.
[26] X. Zhao, L. Dai, Q. Qin, F. Pei, C. Hu, N. Zheng, Self-supported 3D PdCu alloy nanosheets as a bifunctional catalyst for electrochemical reforming of ethanol, Small 13 (2017) 1602970.
[27] H. Li, H. Li, W.-L. Dai, W. Wang, Z. Fang, J.-F. Deng, XPS studies on surface electronic characteristics of Ni-B and Ni-P amorphous alloy and its correlation to their catalytic properties, Appl. Surf. Sci. 152 (1999) 25–34.
[28] T. Li, C. Zhu, X. Yang, Y. Gao, W. He, H. Yue, H. Zhao, Co_3O_4 nanoneedle@ electroactive nickel boride membrane core/shell arrays: a novel hybrid for enhanced capacity, Electrochim. Acta 246 (2017) 226–233.
[29] D. He, L. Zhang, D. He, G. Zhou, Y. Lin, Z. Deng, X. Hong, Y. Wu, C. Chen, Y. Li, Amorphous nickel boride membrane on a platinum-nickel alloy surface for enhanced oxygen reduction reaction, Nat. Commun. 7 (2016) 12362.
[30] N. He, Y. Gong, Y. Yang, Y. Wang, C. Qin, R. Wang, J. Liu, T. Qi, An effective Pd@ Ni-B/C anode catalyst for electro-oxidation of formic acid, Int. J. Hydrogen Energy 43 (2018) 3216–3222.
[31] X. Cui, P. Xiao, J. Wang, M. Zhou, W. Guo, Y. Yang, Y. He, Z. Wang, Y. Yang, Y. Zhang, Z. Lin, Highly branched metal alloy networks with superior activities for the methanol oxidation reaction, Angew. Chem. Int. Ed. 56 (2017) 4488–4493.